International Journal of Bioprinting

RESEARCH ARTICLE

Zn-doped chitosan/alginate multilayer coatings on porous hydroxyapatite scaffold with osteogenic and antibacterial properties

Zhijing He[1,2†], Chen Jiao[1,2†], Junnan Wu[1,2], Jiasen Gu[1,2], Huixin Liang[3], Lida Shen[1,2,4*], Youwen Yang[4*], Zongjun Tian[1,2,4], Changjiang Wang[5], Qing Jiang[6]

[1]Institute of Additive Manufacturing (3D Printing), Nanjing University of Aeronautics and Astronautics, Nanjing, 210016, China

[2]College of Mechanical and Electrical Engineering, Nanjing University of Aeronautics and Astronautics, Nanjing, 210016, China

[3]State Key Laboratory of Pharmaceutical Biotechnology, Nanjing University Medical School Affiliated Nanjing Drum Tower Hospital, Nanjing, 210008, China

[4]Institute of Additive Manufacturing, Jiangxi University of Science and Technology, Ganzhou, 341000, China

[5]Department of Engineering and Design, University of Sussex, Brighton, BN1 9RH, United Kingdom

[6]State Key Laboratory of Pharmaceutical Biotechnology, Division of Sports Medicine and Adult Reconstructive Surgery, Department of Orthopedic Surgery, Nanjing Drum Tower Hospital, The Affiliated Hospital of Nanjing University Medical School, Nanjing, 210008, China

[†]These authors contributed equally to this work.

***Corresponding authors:**
Lida Shen
(ldshen@nuaa.edu.cn)
Youwen Yang
(yangyouwen@jxust.edu.cn)

Citation: He Z, Jiao C, Wu J, *et al*., 2023, Zn-doped chitosan/alginate multilayer coatings on porous hydroxyapatite scaffold with osteogenic and antibacterial properties. *Int J Bioprint*, 9(2): 668. https://doi.org/10.18063/ijb.v9i2.668

Received: September 7, 2022

Accepted: October 21, 2022

Published Online: January 13, 2023

Abstract

Porous hydroxyapatite (HA) scaffolds prepared by three-dimensional (3D) printing have wide application prospects owing to personalized structural design and excellent biocompatibility. However, the lack of antimicrobial properties limits its widespread use. In this study, a porous ceramic scaffold was fabricated by digital light processing (DLP) method. The multilayer chitosan/alginate composite coatings prepared by layer-by-layer method were applied to scaffolds and Zn^{2+} was doped into coatings in the form of ion crosslinking. The chemical composition and morphology of coatings were characterized by scanning electron microscope (SEM) and X-ray photoelectron spectroscopy (XPS). Energy dispersive spectroscopy (EDS) analysis demonstrated that Zn^{2+} was uniformly distributed in the coating. Besides, the compressive strength of coated scaffolds (11.52 ± 0.3 MPa) was slightly improved compared with that of bare scaffolds (10.42 ± 0.56 MPa). The result of soaking experiment indicated that coated scaffolds exhibited delayed degradation. *In vitro* experiments demonstrated that within the limits of concentration, a higher Zn content in the coating has a stronger capacity to promote cell adhesion, proliferation and differentiation. Although excessive release of Zn^{2+} led to cytotoxicity, it presented a stronger antibacterial effect against *Escherichia coli* (99.4%) and *Staphylococcus aureus* (93%).

Keywords: Porous hydroxyapatite scaffold; Multi-layer polymer coating; Zn doping; Osteogenic property; Antibacterial property

1. Introduction

Skeleton supports human body and protects other vulnerable internal organs, and plays a key role in blood production and mineral storage[1-3]. To ensure a healthy skeletal system, bones are in a constant process of remodeling to adjust to mechanical injuries and tiny lesions. However, once the bone defects exceed the critical size that the bone can no longer repair itself, bone substitutes would be needed for healing purposes[4,5]. Since the traditional bone substitutes, including autologous bone and allogeneic bone, were unable to fulfill therapeutic requirements, synthetic bone substitutes have gradually become the focus of research[6]. Calcium phosphate (CaP) bioceramics were one of the earliest bone repair materials in relevant researches because of its biocompatibility and osteoblastic induction properties[7-9]. Nonetheless, pure CaP bioceramics showed poor mechanical and antimicrobial properties, which can be improved by modification[10,11].

In view of the increase of bone transplant failure cases caused by infection every year, antimicrobial property has become one of the most desired properties of bone substitutes[12,13]. Furthermore, due to the misuse of antibiotics for years, drug-resistant bacteria have also become another challenge[14,15]. Metal ions such as Ag^{+}, Zn^{2+}, and Cu^{2+} have shown the ability to kill bacteria and are unlikely to cause mutations in pathogenic bacteria[16,17]. Therefore, the doping of appropriate content of metal elements to scaffolds to kill bacteria in situ became the most adopted antibacterial strategy at present. In particular, it has been proven that Zn^{2+} ions not only possessed reliable antibacterial activity, but also could promote osteoblastogenesis[18,19]. However, once the release rate of Zn^{2+} ions exceeds the safety limits, the scaffolds will become toxic to normal cells such as osteocyte[20]. Some researchers gave priority to osteogenic activity at the expense of antibacterial effect[21,22]. The others studied the addition of other substances to offset the cytotoxicity of Zn^{2+}[23,24]. Considering the fact that the perioperative period is associated with high incidence of infection[25,26], initial antibacterial property is more important than long-term antibacterial property. On that basis, a balanced strategy is proposed in this paper, which is to control the release rate of Zn^{2+} from scaffolds by preparing coatings with different Zn^{2+} contents layer by layer, so as to increase the killing rate of bacteria in the initial stage after implant surgery and to strengthen the osteogenic property in the later stage. Moreover, to obtain such multilayer coating, polymer is chosen as the most appropriate material.

Chitosan and sodium alginate, as biodegradable natural polymers, have been widely developed in bone tissue engineering domains due to outstanding biocompatibility and bioabsorbability[27,28]. The positively charged amino group in chitosan can generate electrostatic interaction with the negatively charged carboxyl group in sodium alginate. Therefore, multilayer polymer coatings can be constructed by layer-by-layer method[29,30]. Besides, sodium alginate can be crosslinked with divalent metal ions to gelation, and the metal ions are stably loaded into the multilayer coatings[31].

In this study, porous hydroxyapatite (HA) bioceramic scaffolds was prepared by digital light processing (DLP) method, and chitosan/sodium alginate polymer coatings were added to scaffolds by layer-by-layer method. Next, Zn^{2+} ions were doped where the ion concentrations were changed layer by layer to achieve a stable and controllable release. Finally, the balance between antimicrobial properties and biological properties was achieved.

2. Materials and methods

2.1. Preparation of porous scaffolds

The detailed preparation process of HA porous scaffolds is described as follows. The first step was to prepare the slurry. HA powders (Aladdin, China) and photosensitive resin (Shanghai, China) were mixed at a mass ratio of 1:1.1, with 3 wt.% of dispersant (Shanghai, China). All raw materials were put into a vacuum disperser, and the slurry was obtained after stirring at 1100 rpm for 30 min. Next, a self-developed DLP printer was used to fabricate the green bodies. The porous scaffold model was designed using Magics 23.0 software (the average pore size was ~1000 μm). According to the experimental requirements, the larger cuboid scaffolds ($9 \times 9 \times 13.5$ mm^3) were prepared for mechanical test, the smaller cuboid scaffolds ($9 \times 9 \times 4.5$ mm^3) were prepared for biological test, and the cylindrical scaffolds ($\Phi 4.5 \times 4.5$ mm^3) were prepared for inhibition zone test. After washing and drying, the ceramic green bodies were debinded and sintered at 1500°C for 3 h; detailed temperature curves were shown in the previous research[32]. The fabrication process is shown in Figure 1.

2.2. Preparation of coatings

The chitosan (Aladdin, China) was dissolved in 0.2% acetic acid (Aladdin, China) solution with the concentration of 2 g/L. The sodium alginate (Aladdin, China) was dissolved in deionized water with the concentration of 2 g/L. Meanwhile, four different crosslinking solutions containing increasing concentrations of $ZnCl_2$ solution (0, 0.25, 0.5, and 1 g/L) were prepared, and $CaCl_2$ of variable concentration was added to adjust the total metal ion concentration to 2 g/L. Subsequently, the HA scaffolds were immersed in the alginate solution, chitosan solution, and one kind of crosslinking solution for 5 min. After each soaking process, the scaffolds were cleaned with distilled

water to remove the uncrosslinked solution and then placed in a conventional oven at 60°C for 2 min. Then, the above-mentioned soaking process was repeated until all the coatings were prepared. The coating process is shown in Figure 2. Four kinds of scaffolds with different coatings were named in accordance with the content of Zn^{2+}, namely, CHA-0, CHA-L, CHA-M, and CHA-H, respectively. Bare scaffold for comparison was named HA. Another specific group, denoted as CHA-G, with gradient coatings was also prepared, in which the Zn^{2+} concentrations of the inner two layers, the middle two layers and the outer two layers were 0.25 g/L, 0.5 g/L, and 1 g/L. The default number of coating layers was 6.

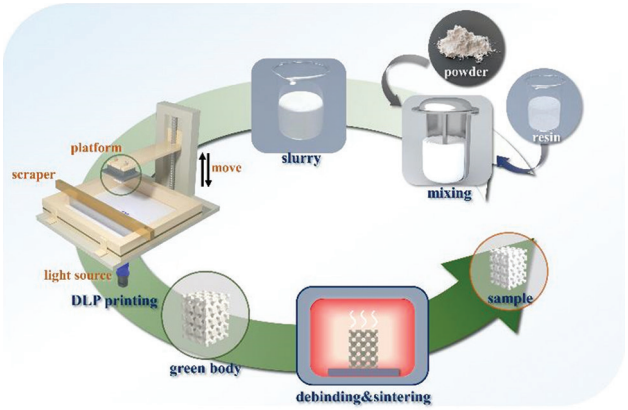

Figure 1. Schematic diagram of porous ceramic scaffold digital light processing additive manufacturing.

2.3. Characterization of scaffolds

The scanning electron microscope (SEM, SU5000, Hitachi Instruments, Japan) was used to analyze the surface and cross section morphologies of the samples. The energy dispersive X-ray (EDX, ULTIMATELYMAX40, Oxford, UK) was used to detect elemental distribution of the coatings. The SEM images of HA scaffold surfaces were statistically analyzed by ImageJ software, and the particle size of HA powders was analyzed with laser granularity analytical instrument (MS2000, Malvin, UK). The X-ray diffraction spectra (XRD) of HA powders and HA scaffolds were obtained on the SmartLab (Rigaku, Japan). The chemical composition and chemical state of the coatings were measured by X-ray photoelectron spectroscopy (XPS; ESCA Xi+, ThermoFischer, USA), and the Avantage software was used for data processing. A universal tester (Zwick-Z250, Germany) was used to test the compressive strength of bare scaffolds and the coated scaffolds, and the crosshead loading speed was 0.1 mm/min. The compressive modulus was obtained from the stress and strain curves[33].

2.4. *In vitro* degradation assays

The HA, CHA-0, and CHA-H samples were immersed in simulated body fluid (SBF, pH=7.4; Scientific Phygene, China) at 37°C, and the ratio of scaffold mass to solution volume was 5 g/L. After 14 days, the apatite deposition on the scaffolds was observed by SEM. To evaluate the effect of coating on degradation property of scaffolds, the HA,

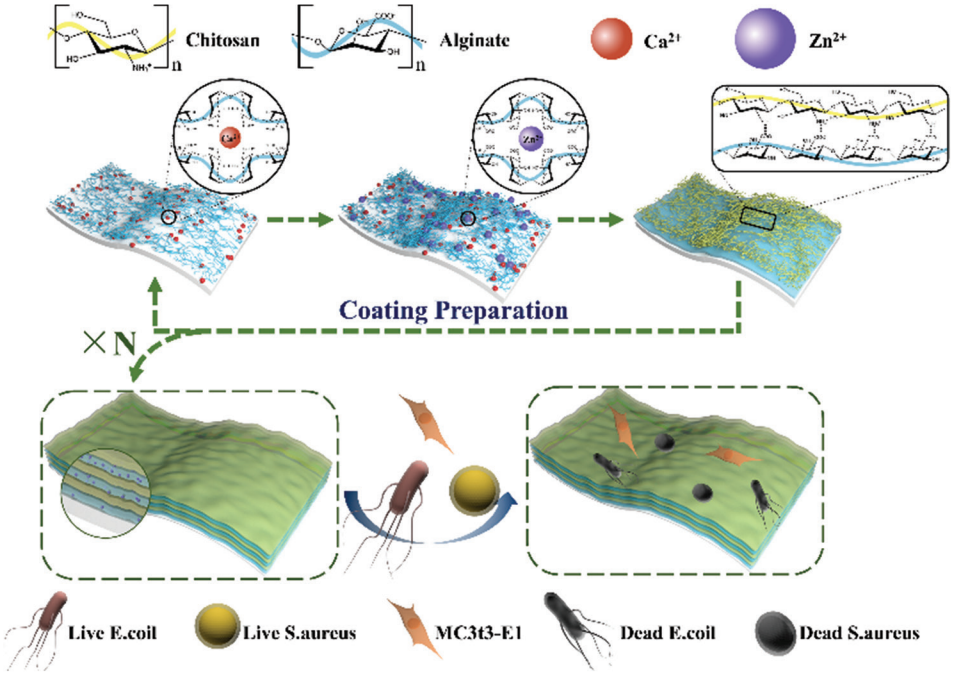

Figure 2. Formation and reaction mechanism of multilayer coatings containing Zn^{2+}.

CHA-M, CHA-M (with 3-layer coating), and CHA-M (with 9-layer coating) were soaked in Tris-HCl buffer solution (pH 7.4; Scientific Phygene, China) with a scaffold mass to solution volume was 5 g/L at 37°C for 1, 2, 3, and 4 weeks. The solution was replaced with fresh tris-HCl solution every 7 days. After a predetermined soaking period, each sample was completely dried and weighed (W_b). The relative mass loss at time b was calculated as: Weight loss = $(W_a\text{-}W_b)/W_a \times 100\%$. W_a was the initial mass of the scaffold. A pH meter was used to measure the pH value in solution.

2.5. Bioactivity *in vitro* assessment

Mouse calvarial pre-osteoblast cell line MC3T3-E1 (MC3T3-E1; Institute of Life Science Cell Culture Center, Shanghai, China) was used in the experiment. The cell growth medium was AMEM (Wisent, Canada) containing 10% fetal bovine serum (Gibco, USA) and 1% penicillin/streptomycin (Wisent, Canada). After being resuscitated from frozen storage, the cells were cultured in incubator at 37°C with 5% CO_2. The medium was replaced every 2 – 3 days.

2.5.1. Cytotoxicity test by live/dead staining

Before the test, all samples were sterilized by autoclave boiler (Shenan, Shanghai, China). Then, pre-osteoblasts (5×10^4 cells/mL) were inoculated directly on the scaffolds. After 4 days of incubation, the scaffolds were stained with Live/Dead Double Staining Kit (Beyotime, China), and then, the staining results were observed under a confocal laser scanning microscope (LSM710, Zeiss, Germany).

2.5.2. Cell proliferation and attachment

Cells (5×10^4 cells/well) were seeded onto scaffolds in 24-well plates. After culturing for 1, 4, and 7 days, the samples were washed three times with phosphate-buffered saline (PBS; Wisent, Canada), followed by 10% Cell Counting Kit-8 solution (CCK-8, diluted with medium; Beyotime, China), which was used for replacing the original medium and incubation for another 2 h. The cells grown in the blank well plate were defined as the control. Then cell viability was measured on a microplate reader (Multiskan FC, Thermo Fisher Scientific, USA) at 450 nm. To examine the cell morphology on scaffolds, the scaffolds were disposed by DAPI (4′,6-diamidino-2-phenylindole, Beyotime, China) and Actin-Tracker Green (Beyotime, China) after 4 days of co-culture. Fluorescent images of cells on scaffolds were observed under a confocal laser scanning microscope.

2.5.3. Cell differentiation

The cells (10^4 cells/mL) were cultured with HA, CHA-0, CHA-L, CHA-M, CHA-H, and CHA-G in 12-well plate. After 14 days of culture, the alkaline phosphatase assay kit (Beyotime, China) was used to measure alkaline phosphatase (ALP) activity, and the optical density (OD) value was measured with a microplate reader at 405 nm. Cellular samples were stained with BCIP/NBT Alkaline Phosphatase Color Development Kit (Beyotime, China), after being fixed with 4% paraformaldehyde for 20 min.

After 21 days of incubation, the samples were stained using the Alizarin Red S Staining Kit for Osteogenesis (Beyotime, China) for 30 min, followed by a rinse with distilled water. Then, an inverted optical microscope (CKX53, Olympus, Japan) was used to observe the stained cells. Afterwards, the 10% (w/v) cetylpyridinium chloride (diluted with PBS; Aladdin, China) was used to quantify the Alizarin red staining (ARS). The absorbance was measured at 562 nm. In addition, the amount of Zn^{2+} released from Zn-doped samples in the collected medium was detected using commercial kits (Zinc, China).

2.6. Antibacterial assay

The antibacterial properties of HA, CHA-0, CHA-L, CHA-M, and CHA-H were assessed against Gram-negative *Escherichia coli* (*E. coli*, ATCC 25922) and Gram-positive *Staphylococcus aureus* (*S. aureus*, ATCC 29213). Before the test, the bacteria on logarithmic phase were dispersed into PBS, and the concentration of bacterial suspension was adjusted using a microplate reader (10^8 CFU/mL; OD_{600}=0.1).

Disk diffusion method was used to qualitatively evaluate antibacterial properties of samples. 100 μL of the bacterial suspension (10^7 CFU/mL) were equably spread over a 90 mm agar plate, followed by dispersedly placing the discoid samples onto the plate and culturing in an incubator with a humidity of about 90% at 37°C for 24 h. Afterward, the zone of inhibition was photographed.

Plate colony-counting method was applied to quantificationally evaluate the antibacterial activities. The samples were exposed to bacterial suspension (10^6 CFU/mL) and then incubated on a shaker for 2 h and 8 h at 37°C. The group without scaffold was considered a control. After the appropriate proportion of dilution, the bacterial suspension was inoculated onto solid medium and then cultured until colonies were formed. The antibacterial efficiency was computed based on following equation:

$$\text{Antibacterial efficiency (\%)} = (A_c - A_s)/A_c \times 100\%$$

Where A_c and A_s are the bacterial colony numbers of control and sample groups, respectively.

2.7. Statistical analysis

The data were processed using Origin 2018 software (Originlab, USA). Values were expressed as means ±

standard deviation (SD), and significance of data was determined by $P < 0.05$. Besides, the data with probability less than 0.05 ($P < 0.05$), 0.01 ($P < 0.01$), and 0.001 ($P < 0.001$) were represented by *, **, and ***, respectively.

3. Results and discussion

3.1. Characterization of scaffolds

3.1.1. Surface morphology

The comparison of unsintered and sintered porous ceramic scaffold is shown in Figure 3A. After sintering, the photosensitive resin was removed completely, resulting in a considerable volume contraction of the porous scaffold, and the average linear shrinkage rate was 30%. The XRD patterns of the ceramic powder and bare scaffolds are displayed in Figure 3B. The main component of the scaffold was HA (# 70-0566), and no significant phase transition occurred during sintering. Compared with the size distribution of raw HA powders (Figure 3C), the particle size of HA scaffold surface mainly distributed from 10 to 15 μm (Figure 3D), which indicated that the grain grew normally. In addition, the SEM results of surface micrographs of HA scaffold showed that the grains were compacted (Figure 3D).". As for the morphology of coating, the coating materials penetrated into the gaps between ceramic particles and a smoother surface was then obtained (Figure 3E). The cross-section morphology of the scaffold with coatings is shown at the top right corner of Figure 3E. A multilayered structure was clearly displayed, and the total thickness of the coating was 6.7 μm, from which it could be inferred that the thickness of single coating was about 0.74 μm. In addition, the change of Zn concentration in the coating had no effect on its morphology. Finally, the EDS mapping of Ca and Zn elements in the coating of the CHA-H scaffold confirmed that Zn^{2+} was homogeneously distributed (Figure 3G and 3H).

3.1.2. XPS characterization

To investigate the detailed chemical composition of the coatings, the XPS analyses were performed. Figure 4A shows the total XPS spectra of CHA-0 and CHA-H groups, which were typical among all groups. The elements contained in the raw material, such as C, N, O, Ca, and Zn, could be detected in CHA-H, and all of these elements

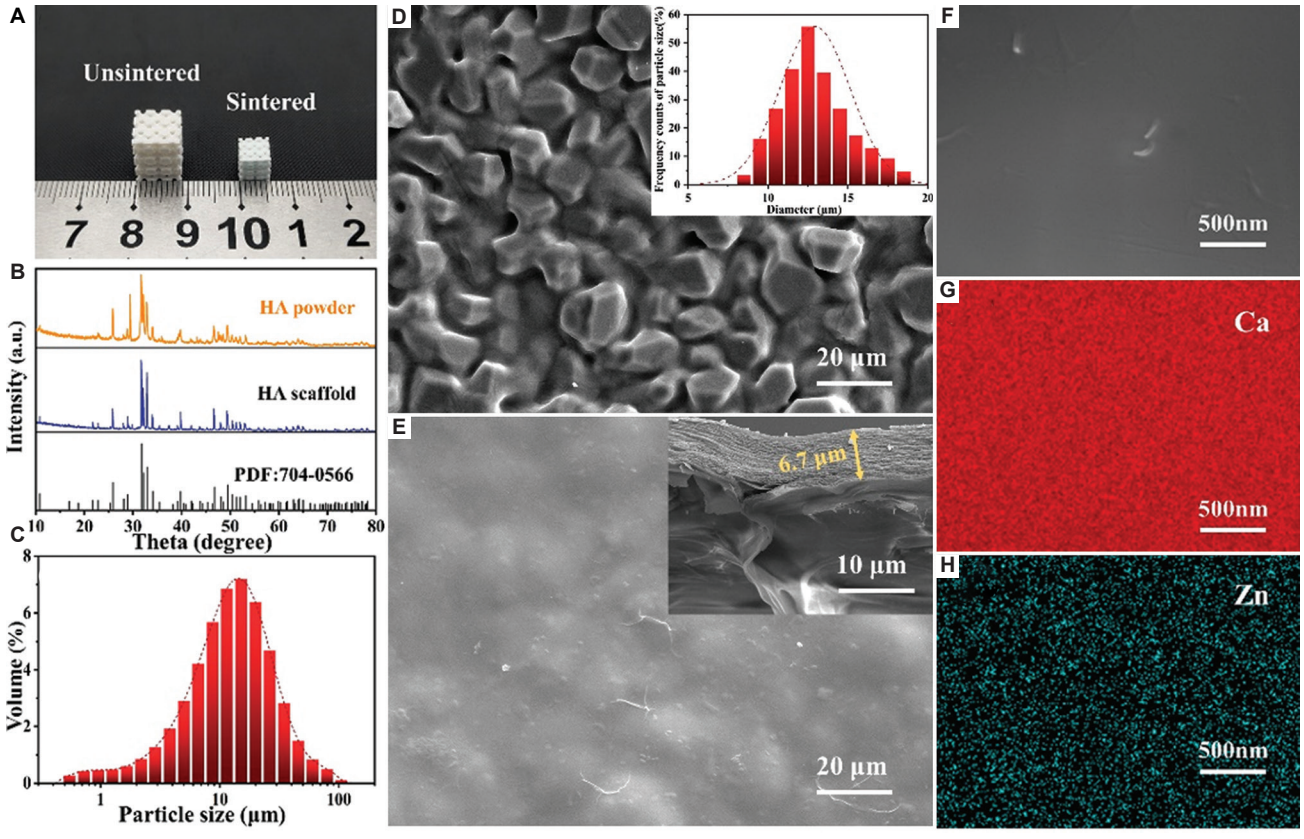

Figure 3. (A) Images of unsintered and sintered hydroxyapatite (HA) scaffolds. (B) X-ray diffraction spectra of HA powder and scaffold. (C) Particle size distribution of ceramic powders. (D) Scanning electron microscope (SEM) image of HA scaffold; the inset image shows the size distribution of ceramic particle on the scaffold surface. (E) SEM image of HA scaffold with coatings; the inset image shows the cross section of coatings. (F) High-magnification SEM image of coatings. (G and H) EDS mapping of Ca and Zn on CHA-H sample.

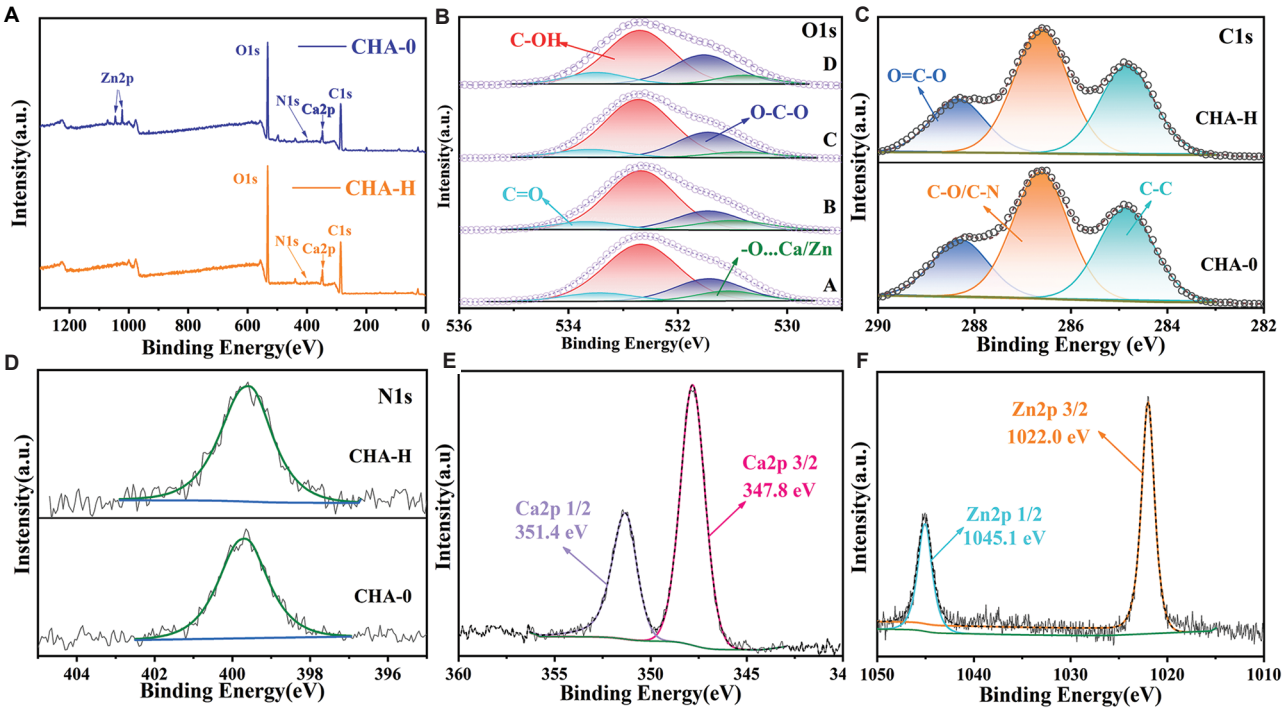

Figure 4. (A) The survey XPS spectra of CHA-0 and CHA-H. (B) O 1s spectra, A – D: CHA-0, CHA-L, CHA-M, and CHA-H, respectively. (C) C 1s and (D) N 1s spectra of CHA-0 and CHA-H, respectively. (E) Ca 2p spectra and (F) Zn 2p spectra of CHA-H.

were also detected from CHA-0, except Zn. N was only ascribed to chitosan in the coating, so the content was low and the spectral peak was not obvious. Furthermore, $CaCl_2$ and $ZnCl_2$ were employed as crosslinking agent, in which divalent metal ions interact strongly with carboxyl groups of sodium alginate. However, there were no groups in the coating that could interact with Cl^- ions, so its content was almost negligible. Similarly, the Na^+ ions in sodium alginate were replaced by Ca^{2+} and Zn^{2+} ions, resulting in an insignificant spectral peak.

The O 1s XPS spectra (Figure 4B) were deconvoluted into 4 peaks near 533.5, 532.7, 531.5, and 531 eV, corresponding to C=O, C-OH, C-O-C, and O…Zn/Ca[34]. The peak of O…Zn/Ca shifted rightward with the increase of Zn concentration in coatings caused by the different interaction forces of Zn^{2+} and Ca^{2+} on carboxyl groups, and the detailed values for CHA-0, CHA-L, CHA-M, and CHA-H groups were 531.1, 530.95, 530.85, and 531.7 eV, respectively. The C 1s spectra are shown in Figure 4C. They were deconvoluted into three principal peaks near 288.2, 286.6 and 284.8 eV, which were assigned O-C=O, C-O/C-N, and C-C bonds, respectively[35,36]. Figure 4D showed that the N 1s spectra and the peaks near 399.8 eV were attributed to amidogen groups ($-NH^{3+}$)[37]. CHA-0 and CHA-H were selected because they were most likely to differ, and in fact all samples had similar C 1s and N 1s spectra. In Figure 4E and 4F, the binding energies of 351.4 and 347.8 eV were classified to the Ca 2p1/2 and Ca 2p3/2 orbitals of the Ca^{2+} in CHA-0 group, while 1045.1 and 1022 eV were classified to the Zn 2p1/2 and Zn 2p3/2 orbitals of the Zn^{2+} in CHA-H group[38]. The relative atomic ratios of Zn and Ca elements on the coating surface are given in Table 1. There were some acceptable differences between experimental and theoretical values caused by experimental errors. Therefore, the concentration of Zn ions in the coating could be adjusted by changing the proportion of Ca/Zn ions in the solution without changing the concentration of the crosslinking agent solution.

3.2. Mechanical properties of samples

To evaluate the effect of coating on mechanical properties of scaffolds, the compressive strength and compressive modulus values of the bare scaffold and coated scaffold are compared. As shown in Figure 5, compressive strength of bare scaffold was 10.42 ± 0.56 MPa, while that of the coated scaffold was 11.52 ± 0.3 MPa. These results suggested that the coating could improve the mechanical properties of scaffolds, although the improvement was not significant. The reasons could be attributed to two components. On the one hand, although the mechanical strength of the polymer coating material was extremely poor, it could still play a certain supporting role under pressure[39]. On

the other hand, it was inevitable that some defects would appear on the scaffold surface during the preparation process. The addition of the adhesive coating properly filled these defects, thus avoiding the premature collapse of scaffolds.

3.3. Degradation properties of samples

Numerous studies have shown that HA scaffolds could induce apatite deposition on the surface in SBF, which was related to the bioactivity properties of scaffolds[40,41]. The HA, CHA-0, and CHA-H scaffolds were soaked in the SBF for 14 days at 37°C, and then the surface morphologies were observed by SEM. As showed in Figure 6A, coralloid deposits were formed on the surface of the HA scaffold. The EDS results (Figure 6B) confirmed that the deposits were calcium phosphate, and the calcium to phosphorus ratio was 1.37. Studies have suggested that calcium phosphate could be classified as HA when the Ca/P ratio was between 1.3 and 2.0[42]. As for the scaffold with coating (Figure 6C–F), the apatite deposits on the surface were less and appeared as spherical clusters, indicating that the addition of coating inhibited the deposition of apatite to a certain extent. In addition, the EDS results showed that the Ca/P ratio of the coated scaffold was significantly higher than that of the HA scaffold, which can be attributed to the fact that the penetration depth of EDS detection was too large to be interfered by the elements of the sample itself. In particular, it was interesting to note that the Ca/P ratio of CHA-H was higher than that of CHA-0, even though the calcium content in the coating of CHA-H group was lower than that of CHA-0 group. It indicated that the higher the Zn content in the coating, the higher the Ca/P ratio in the induced apatite deposition layer, which may be attributed to the complex nucleation mechanism of apatite[43]. Moreover, the surface morphology of CHA-0 and CHA-H samples also indicated that the coating with higher Zn concentration might have a stronger ability to induce apatite deposition.

Table 1. Planned and experimentally obtained molar ratios of Ca:Zn in coatings.

Sample	Planned (in the crosslinking agent solution)		XPS elemental analysis (in samples)
	Mass ratio of $CaCl_2$:$ZnCl_2$	Molar ratio of Ca^{2+}:Zn^{2+}	Molar ratio of Ca:Zn
CHA-0	0:1	0:1	0:1
CHA-H	1:1	1:1.23	1:1.31
CHA-M	1:3	1:3.68	1:3.48
CHA-L	1:7	1:8.58	1:6.73

To evaluate the effect of coatings on the degradation of scaffolds, the bare HA scaffold and the CHA-M scaffolds with different number of coating layers (3, 6, and 9 layers, respectively) were immersed in Tris-HCl for 7, 14, 21, and 28 days. The degradation curves are shown in Figure 7A, The HA scaffold had the highest mass loss of 2.93% among all groups after 4 weeks. For coated scaffolds, the mass loss rate showed a dependence on the number of coating layers. As the number of coating layers increased, the weight loss rate of scaffolds was slower, showing a delayed effect. Consequently, the addition of coating inhibited the degradation of scaffolds.

Figure 7B showed the variation of pH values of Tris-HCl solution after soaking the samples. During the whole soaking process, except for the CHA-M (9), the pH value of the other groups decreased first and then tended to be stable, but the reasons were not exactly the same. For the HA scaffold, its degradation products were weakly alkaline, while the deposition of apatite would consume the hydroxide ions in the solution, leading to a decrease of pH value[44,45]. Consequently, the pH value of the immersion solution showed a state of fluctuation. As for the coated scaffolds, in addition to the effect caused by apatite deposition, the decrease of the pH value of the solution might be due to the trace residue of acetic acid introduced

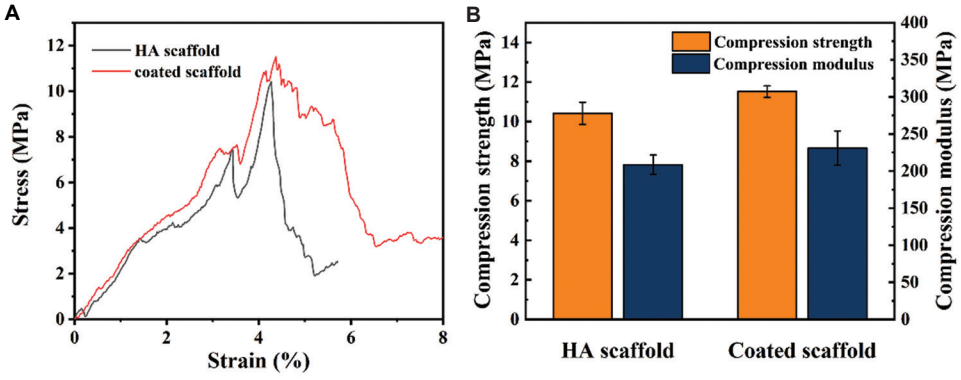

Figure 5. (A) Compression stress-strain curves of the scaffolds. (B) Compressive strength and compressive modulus of the scaffolds.

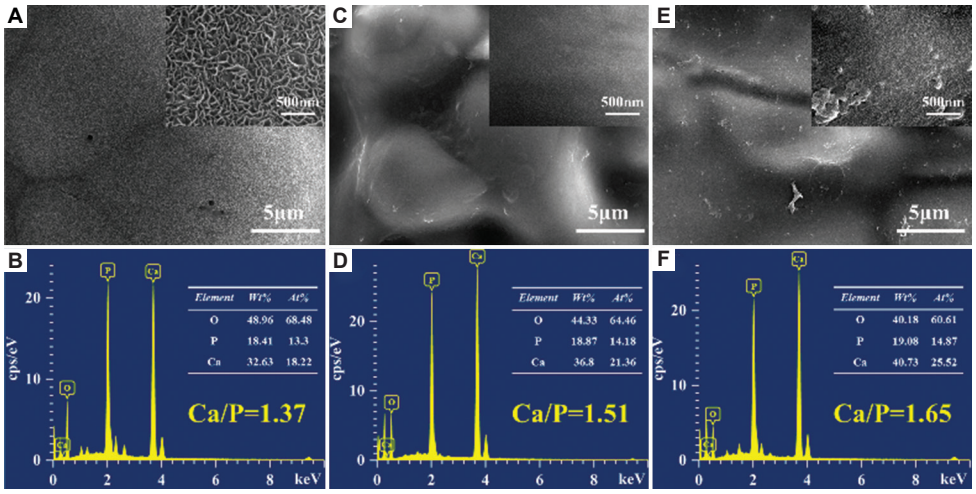

Figure 6. Scanning electron microscope images of mineral deposited on (A) hydroxyapatite (HA), (C) CHA-0, and (E) CHA-H scaffolds in SBF for 14 days. EDS analyses of the surface sediment of (B) HA, (D) CHA-0, and (F) CHA-H scaffolds are also shown.

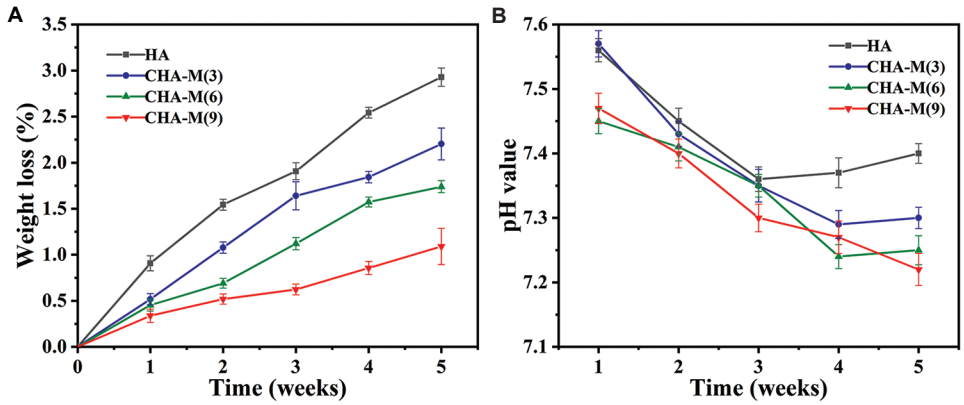

Figure 7. Weight loss (A) and pH value (B) of scaffolds after soaking in Tris-HCl for different durations (the solution refreshed every week).

during the preparation of the coating. Although the pH value of the solution after soaking the bare HA scaffold was on average higher than that of coated scaffolds, these differences were not significant. Overall, the coating had little effect on the pH of body fluid environment. In particular, the pH values of all groups were always higher than 7, showing weak alkalinity, which has been proven to be beneficial to the growth of osteoblasts[46].

3.4. *In vitro* biocompatibility properties

Although the addition of the coating inhibited apatite formation, it was not the sole criterion for biological activity. The viability of MC3T3-E1 cells on days 1, 4, and 7 was evaluated by CCK-8 assay. As shown in Figure 8, the cell proliferation of all groups (except CHA-H) was better than that of blank control group in a time-dependent manner, indicating good biocompatibility of the scaffolds. Furthermore, at each detection node, their proliferative capacities in decreasing order were: CHA-M, CHA-L, HA, and CHA-0 groups. The low cell activity of CHA-H group was caused by high concentration of Zn^{2+} ion, which was toxic to cells.

To further verify biocompatibility of scaffolds, the cell physiological status and survival was observed using fluorescence microscope on day 4. In Figure 9A, the cytoskeleton was displayed as green spots and the nucleus was shown as blue spots. The filopodia and pseudopodia extension of the cell could be conformably observed on all scaffolds except CHA-H, which indicate excellent growth of cells[47]. The cells on CHA-H scaffold surface were smaller and not extended enough. Furthermore, the quantity of cells in each group shown by fluorescence images was basically in accordance with the data of CCK-8 assay. To explore the damage on cells caused by high Zn^{2+} concentration, calcein and propidium iodide staining was performed. As shown in Figure 9B, living cells were green

and dead cells were red. It was found that although the cells on CHA-H scaffold were less due to its low proliferative potential, only a few of them died. For other groups, the dead cells were almost invisible.

3.5. Osteogenesis differentiation

Osteoblasts go through proliferation, differentiation and mineralization, and eventually become mature osteocytes[48]. Therefore, osteogenic differentiation is the key stage of bone regeneration. ALP activity was related to the early osteogenic differentiation[49], and the capacity of cell mineralization, which was evaluated by Alizarin red staining assays, was a marker of late osteogenic differentiation[50]. ALP staining results (purple stain) displayed that ALP was detected in all experimental groups (Figure 10A), and the results of ALP quantitative analysis are presented in Figure 10B. Among all groups, cells inoculated on the CHA-M samples showed the highest level of ALP expression. Interestingly, the ALP activity of CHA-G group was comparable to that of CHA-L group, second only to the CHA-M group. This result corroborated that Zn^{2+} ions released by CHA-H were not sufficient to kill the cells. Therefore, the cell viability was recovered with the decrease of Zn^{2+} ions concentration in the late culture stage. Furthermore, ARS staining and quantitative analysis (Figure 10C and 10D) showed a similar trend as noted in the ALP assay, confirming that Zn-coated scaffolds had better osteogenic potential than bare scaffolds. Finally, Zn^{2+} ions concentration in medium incubated with different samples were investigated, and the results are shown in Figure 11. CHA-H, CHA-M, and CHA-L groups could basically maintain steady release rate of Zn^{2+} ions over time, while CHA-G group showed a marked decreasing tendency, suggesting that multilayer coatings are feasible to control the release of Zn^{2+} ions.

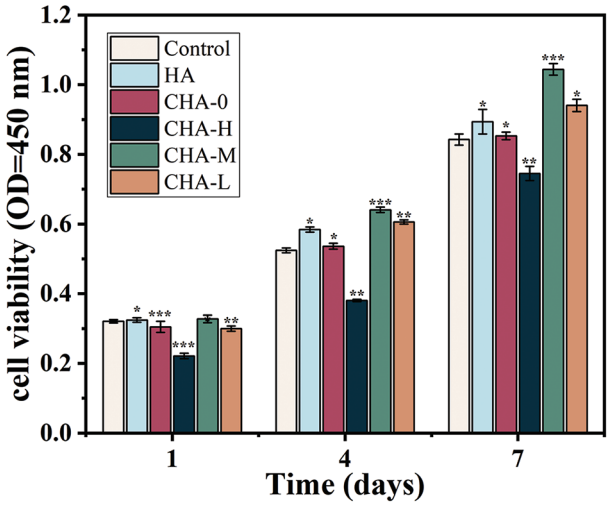

Figure 8. Cell viability of MC3T3-E1 cells after 1, 4, and 7 days of co-culture with samples.

The results of biological experiments indicated that chitosan and sodium alginate coating had good biocompatibility and were non-toxic to cells. The composite polymer had properties similar to extracellular matrix, which was beneficial to cell adhesion. In addition, Zn^{2+} ions were doped into coatings in the form of interaction, ensuring the steady release of ions, and the release rate could be arbitrarily controlled by means of preparing the coating layer by layer. As a trace element in human body, Zn^{2+} ions were conducive to the proliferation and differentiation of osteoblasts at appropriate concentration. Although high Zn^{2+} concentration of ions could reduce cell viability, the fact that it could induce stronger antibacterial activity should warrant more investigation.

3.6. Antibacterial activity

Bacterial infection represents one the major factors of transplant failure. Therefore, research on antibacterial

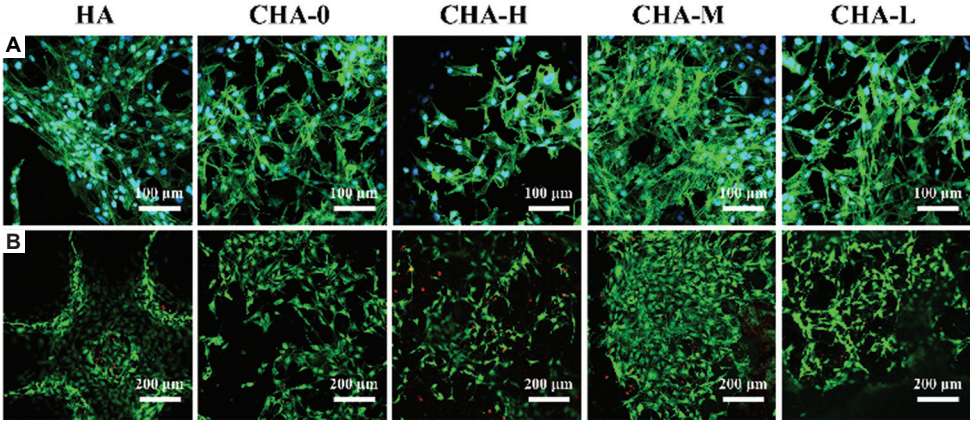

Figure 9. Fluorescent images of (A) phalloidin/DAPI and (B) calcein/PI staining of cells incubated with different scaffolds for 4 days.

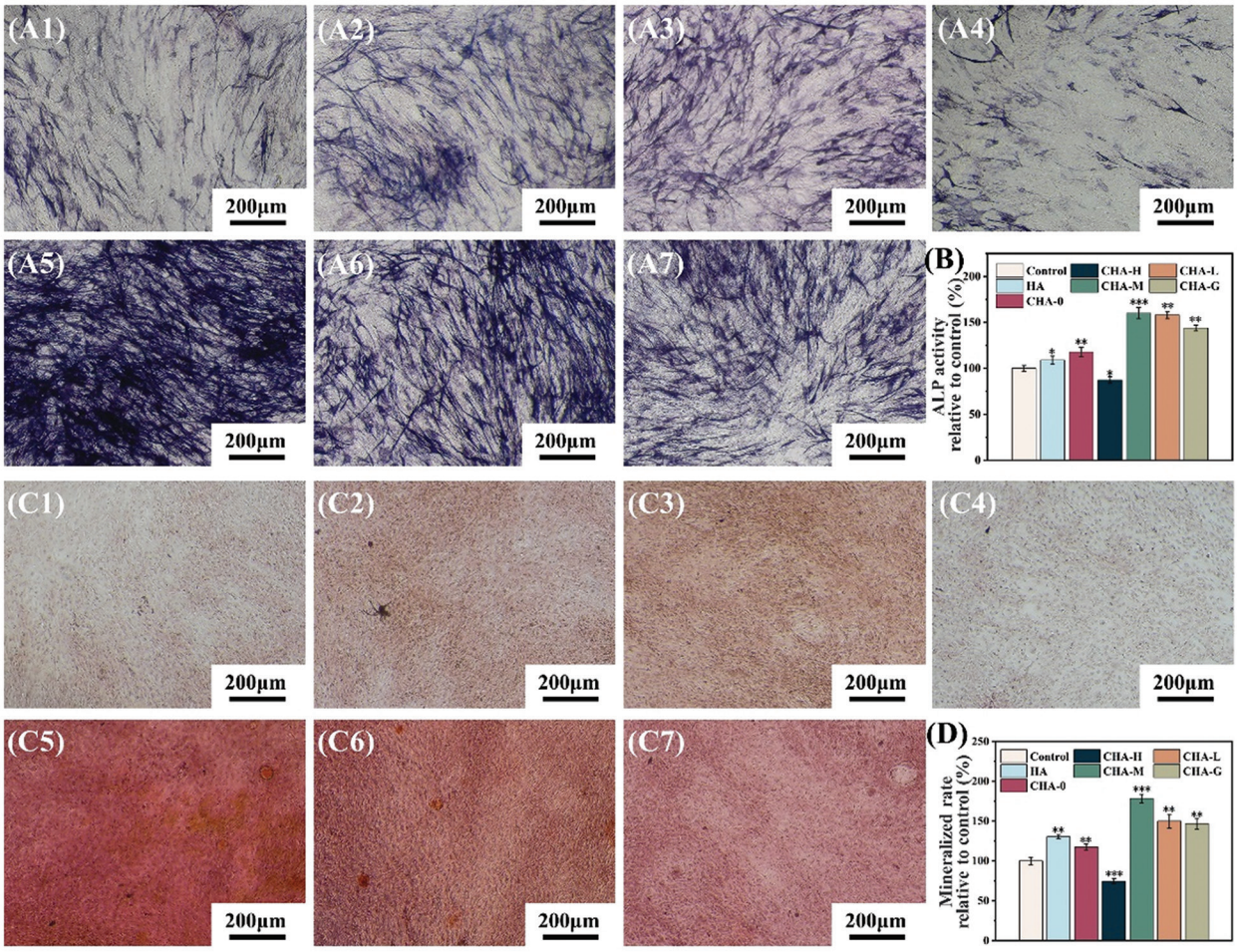

Figure 10. (A) Alkaline phosphatase (ALP) staining of cells co-cultured with different scaffolds for 14 days, A1 – A7: control, HA, CHA-0, CHA-H, CHA-M, CHA-L, and CHA-G, respectively. (B) Quantitative analysis of ALP activity. (C) ARS staining of cells co-cultured with different scaffolds for 21 days, C1 – C7: control, HA, CHA-0, CHA-H, CHA-M, CHA-L, and CHA-G, respectively. (D) Quantitative analysis of mineralized rate.

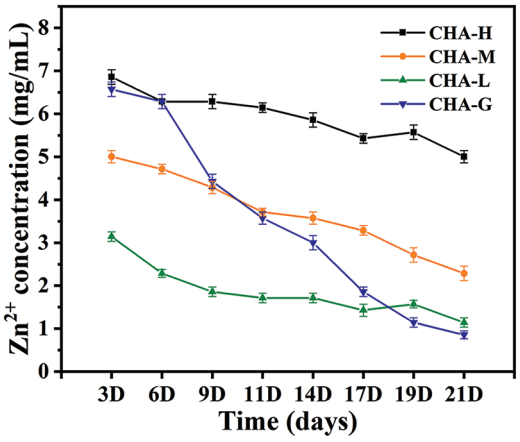

Figure 11. Concentration of Zn^{2+} ions released in cell culture media.

scaffolds has been gaining popularity and attention in recent years. Zn^{2+} ions could kill bacteria by inducing reactive oxygen species, thereby avoiding the deleterious effects of antimicrobial resistance[51]. *E. coli* and *S. aureus*, as the representative of two major categories of bacteria, were chosen to evaluate the antibacterial activity of scaffolds. As shown in Figure 12A, after being exposed to bacterial suspension for 2 h, the inhibition rate of Zn-doped scaffolds showed a dependence on the Zn^{2+} concentration, which were 87.2, 70.8, and 47.8% against *E. coli*, and 73.2, 59.6, and 39.6% against *S. aureus* (the colony count results are shown in Figure 11E and 11F). The HA and CHA-0 scaffold had almost no antibacterial properties, indicating that the antibacterial effect of scaffolds was mainly attributed to Zn^{2+} ions. Furthermore, bacterial mortality rates of all Zn-doped groups increased with the treatment time extended to 8 h, and the rate even reached 99.4% against *E. coli* and 93% against *S. aureus* in CHA-H group. For disk diffusion experiment (Figure 12C and 12D), obvious inhibition zone was observed around the CHA-H

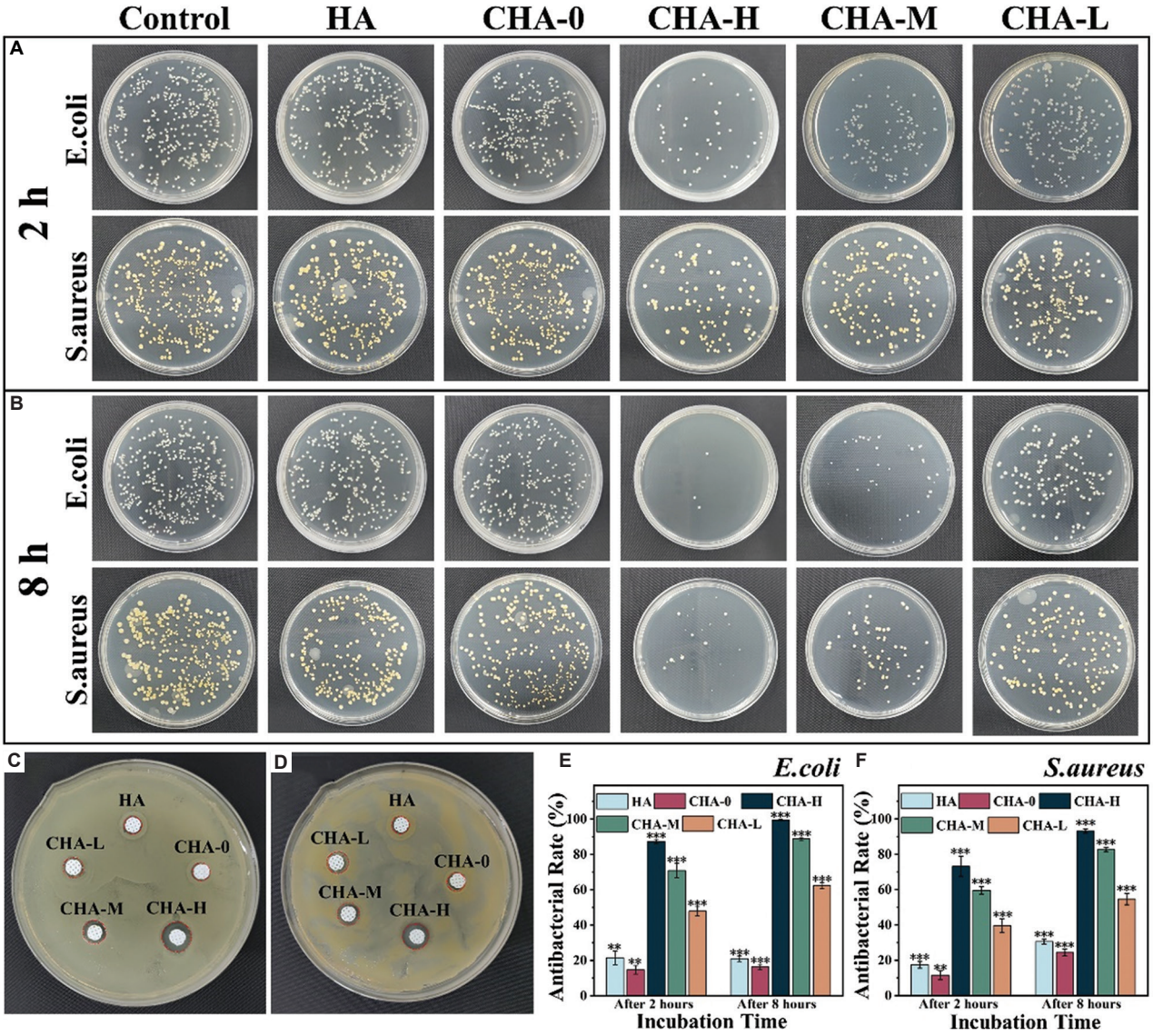

Figure 12. The growth of bacteria on agar plates after being co-cultured with scaffolds for (A) 2 h and (B) 8 h. Inhibition zone of different samples to (C) *Escherichia coli* and (D) *Staphylococcus aureus* was determined by disk diffusion assay. The antibacterial rate against (E) *E. coli* and (F) *S. aureus* was obtained by counting the number of colonies.

scaffold. To sum up, the scaffolds with Zn-doped coating showed great potential to inhibit bacterial infections in tissue engineering.

4. Conclusion

In this paper, we propose a universal, convenient, and reliable preparation method of multilayer coating. The EDS and XPS results demonstrated that as a part of cross-linking agent, Zn^{2+} ions were stably and uniformly doped into the polymer coating, and the content of Zn^{2+} in the coating was subject to the ratio of Ca^{2+}/Zn^{2+} in the crosslinking agent solution. Besides, the coating had little effect on the compressive strength of the scaffold but inhibited the degradation of scaffold to some extent. *In vitro* studies showed that CHA-M group with moderate Zn^{2+} release rate had the best biocompatibility and osteoinductivity. In contrast, the CHA-H group showed the worst biological activity, but excessive Zn^{2+} concentration did not kill the cells completely according to the results of live/dead cell staining. In addition, CHA-H scaffold exhibited outstanding antibacterial activity against *E. coli* and *S. aureus*. Therefore, coatings containing gradient Zn concentrations were specially prepared to reconcile the contradiction between the osteogenic and antimicrobial

properties. Taken together, the multilayer coatings prepared by layer-by-layer method could realize the controllable release of Zn^{2+} and balance the osteogenic and antimicrobial activity, indicating its promising potential in bone tissue engineering.

Acknowledgments

The authors extend their sincere gratitude to those who contributed in instructions and experiments.

Funding

This work was supported by Jiangsu Provincial Key Research and Development Program (No. BE2019002).

Conflict of interest

The authors declare that they have no known competing financial interests or personal relationships that could have appeared to influence the work reported in this paper.

Author contributions

Conceptualization: Zhijing He, Lida Shen
Data curation: Chen Jiao
Formal analysis: Zongjun Tian
Investigation: Changjiang Wang, Qing Jiang
Methodology: Zhijing He, Junnan Wu, Jiasen Gu, Huixin Liang
Supervision: Lida Shen, Zongjun Tian
Project administration: Lida Shen
Validation: Zhijing He, Chen Jiao, Youwen Yang, Changjiang Wang
Visualization: Chen Jiao
Writing – original draft: Zhijing He
Writing – review & editing: Youwen Yang

Ethics approval and consent to participate

Not applicable.

Consent for publication

Not applicable.

Availability of data

The datasets used and analyzed during the present study can be obtained from the corresponding author on request.

References

1. Cheng H, Chawla A, Yang Y, *et al*., 2017, Development of nanomaterials for bone-targeted drug delivery. *Drug Discov Today*, 22: 1336–1350.

   https://doi.org/10.1016/j.drudis.2017.04.021

2. Ferreira AM, Gentile P, Chiono V, *et al*., 2012, Collagen for bone tissue regeneration. *Acta Biomater*, 8: 3191–3200.

   https://doi.org/10.1016/j.actbio.2012.06.014

3. Arrigoni C, Gilardi M, Bersini S, *et al*., 2017, Bioprinting and organ-on-chip applications towards personalized medicine for bone diseases. *Stem Cell Rev Rep*, 13: 407–417.

   https://doi.org/10.1007/s12015-017-9741-5

4. Koons GL, Diba M, Mikos AG, 2020, Materials design for bone-tissue engineering. *Nat Rev Mater*, 5: 584–603.

   https://doi.org/10.1038/s41578-020-0204-2

5. Garcia P, Histing T, Holstein JH, *et al*., 2013, Rodent animal models of delayed bone healing and non-union formation: A comprehensive review. *Eur Cells Mater*, 26: 1–12.

   https://doi.org/10.22203/ecm.v026a01

6. Turnbull G, Clarke J, Picard F, *et al*., 2018, 3D bioactive composite scaffolds for bone tissue engineering. *Bioact Mater*, 3: 278–314.

   https://doi.org/10.1016/j.bioactmat.2017.10.001

7. Aulakh TS, Jayasekera N, Kuiper JH, *et al*., 2009, Long-term clinical outcomes following the use of synthetic hydroxyapatite and bone graft in impaction in revision hip arthroplasty. *Biomaterials*, 30: 1732–1738.

   https://doi.org/10.1016/j.biomaterials.2008.12.035

8. Jeong J, Kim JH, Shim JH, *et al*., 2019, Bioactive calcium phosphate materials and applications in bone regeneration. *Biomater Res*, 23: 4.

   https://doi.org/10.1186/s40824-018-0149-3

9. Zeng JH, Liu SW, Xiong L, *et al*., 2018, Scaffolds for the repair of bone defects in clinical studies: A systematic review. *J Orthop Surg Res*, 13: 33.

   https://doi.org/10.1186/s13018-018-0724-2

10. Mahanty A, Shikha D, 2022, Changes in the morphology, mechanical strength and biocompatibility of polymer and metal/polymer fabricated hydroxyapatite for orthopaedic implants: A review. *J Polym Eng*, 42: 298–322.

    https://doi.org/10.1515/polyeng-2021-0171

11. Vilardell AM, Cinca N, Concustell A, *et al*., 2015, Cold spray as an emerging technology for biocompatible and antibacterial coatings: State of art. *J Mater Sci*, 50: 4441–4462.

    https://doi.org/10.1007/s10853-015-9013-1

12. Przekora A, 2019, Current trends in fabrication of biomaterials for bone and cartilage regeneration: Materials modifications and biophysical stimulations. *Int J Mol Sci*, 20: 435.

    https://doi.org/10.3390/ijms20020435

13. Li F, Li S, Liu Y, *et al*., 2022, Current advances in the roles of doped bioactive metal in biodegradable polymer composite scaffolds for bone repair: A mini review. *Adv Eng Mater*,

24: 2101510.

https://doi.org/10.1002/adem.202101510

14. Sierra MA, Casarrubios L, de la Torre MC, 2019, Bio-organometallic derivatives of antibacterial drugs. *Chemistry*, 25: 7232–7242.

https://doi.org/10.1002/chem.201805985

15. Li B, Webster TJ, 2018, Bacteria antibiotic resistance: New challenges and opportunities for implant-associated orthopedic infections. *J Orthop Res*, 36: 22–32.

https://doi.org/10.1002/jor.23656

16. Godoy-Gallardo M, Eckhard U, Delgado LM, *et al.*, 2021, Antibacterial approaches in tissue engineering using metal ions and nanoparticles: From mechanisms to applications. *Bioact Mater*, 6: 4470–4490.

https://doi.org/10.1016/j.bioactmat.2021.04.033

17. Saidin S, Jumat MA, Amin NA, *et al.*, 2021, Organic and inorganic antibacterial approaches in combating bacterial infection for biomedical application. *Mater Sci Eng C Mater*, 118: 111382.

https://doi.org/10.1016/j.msec.2020.111382

18. Bhattacharjee A, Gupta A, Verma M, *et al.*, 2019, Site-specific antibacterial efficacy and cyto/hemo-compatibility of zinc substituted hydroxyapatite. *Ceram Int*, 45: 12225–12233.

https://doi.org/10.1016/j.ceramint.2019.03.132

19. Yang Y, Zan J, Shuai Y, *et al.*, 2022, *In Situ* growth of a metal-organic framework on graphene oxide for the chemo-photothermal therapy of bacterial infection in bone repair. *ACS Appl Mater Inter*, 14: 21996–22005.

https://doi.org/10.1021/acsami.2c0484121996

20. Wätjen W, Haase H, Biagioli M, *et al.*, 2002, Induction of apoptosis in mammalian cells by cadmium and zinc. *Environ Health Persp*, 110: 865–867.

https://doi.org/10.1289/ehp.110-1241262

21. Lu T, Yuan X, Zhang L, *et al.*, 2021, High throughput synthesis and screening of zinc-doped biphasic calcium phosphate for bone regeneration. *Appl Mater Today*, 25: 101225.

https://doi.org/10.1016/j.apmt.2021.101225

22. Shen J, Chen B, Zhai X, *et al.*, 2021, Stepwise 3D-spatio-temporal magnesium cationic niche: Nanocomposite scaffold mediated microenvironment for modulating intramembranous ossification, *Bioact Mater*, 6: 503–519.

https://doi.org/10.1016/j.bioactmat.2020.08.025

23. Ullah I, Siddiqui MA, Kolawole SK, *et al.*, 2020, Synthesis, characterization and *in vitro* evaluation of zinc and strontium binary doped hydroxyapatite for biomedical application. *Ceram Int*, 46: 14448–14459.

https://doi.org/10.1016/j.ceramint.2020.02.242

24. Wang Q, Tang P, Ge X, *et al.*, 2018, Experimental and simulation studies of strontium/zinc-codoped hydroxyapatite porous scaffolds with excellent osteoinductivity and antibacterial activity. *Appl Surf Sci*, 462: 118–126.

https://doi.org/10.1016/j.apsusc.2018.08.068

25. Campoccia D, Montanaro L, Arciola CR, 2006, The significance of infection related to orthopedic devices and issues of antibiotic resistance. *Biomaterials*, 27: 2331–2339.

https://doi.org/10.1016/j.biomaterials.2005.11.044

26. Gasik M, 2017, Understanding biomaterial-tissue interface quality: Combined *in vitro* evaluation. *Sci Technol Adv Mat*, 18: 550–562.

https://doi.org/10.1080/14686996.2017.1348872

27. Islam MM, Shahruzzaman M, Biswas S, *et al.*, 2020, Chitosan based bioactive materials in tissue engineering applications-A review. *Bioact Mater*, 5: 164–183.

https://doi.org/10.1016/j.bioactmat.2020.01.012

28. Aguero L, Alpdagtas S, Ilhan E, *et al.*, 2021, Functional role of crosslinking in alginate scaffold for drug delivery and tissue engineering: A review. *Eur Polym J*, 160: 110807.

https://doi.org/10.1016/j.eurpolymj.2021.110807

29. Huang C, Fang G, Zhao Y, *et al.*, 2019, Bio-inspired nanocomposite by layer-by-layer coating of chitosan/hyaluronic acid multilayers on a hard nanocellulose-hydroxyapatite matrix. *Carbohyd Polym*, 222: 115036.

https://doi.org/10.1016/j.carbpol.2019.115036

30. Wang R, Sun L, Zhu X, *et al.*, 2022, Carbon nanotube-based strain sensors: Structures, fabrication, and applications. *Adv Mater Technol*, 2022: 2200855.

https://doi.org/10.1002/admt.202200855

31. Hernandez-Gonzalez AC, Tellez-Jurado L, Rodriguez-Lorenzo LM, 2020, Alginate hydrogels for bone tissue engineering, from injectables to bioprinting: A review. *Carbohyd Polym*, 229: 115514.

https://doi.org/10.1016/j.carbpol.2019.115514

32. Jiao C, Xie D, He Z, *et al.*, 2022, Additive manufacturing of Bio-inspired ceramic bone Scaffolds: Structural Design, mechanical properties and biocompatibility. *Mater Design*, 217: 110610.

https://doi.org/10.1016/j.matdes.2022.110610

33. Liang H, Yang Y, Xie D, *et al.*, 2019, Trabecular-like Ti-6Al-4V scaffolds for orthopedic: Fabrication by selective laser melting and *in vitro* biocompatibility. *J Mater Sci Technol*, 35: 1284–1297.

https://doi.org/10.1016/j.jmst.2019.01.012

34. He H, Lian J, Chen C, *et al.*, 2022, Enabling multi-chemisorption sites on carbon nanofibers cathodes by an *in-situ* exfoliation strategy for high-performance Zn-Ion

hybrid capacitors. *Nanomicro Lett*, 14: 106.

https://doi.org/10.1007/s40820-022-00839-z

35. Khan MU, Razak SI, Ansari MN, *et al*., 2021, Development of biodegradable bio-based composite for bone tissue engineering: Synthesis, characterization and *in vitro* biocompatible evaluation. *Polymers* (*Basel*), 13: 3611.

https://doi.org/10.3390/polym13213611

36. Li D, Liu P, Hao F, *et al*., 2022, Preparation and application of silver/chitosan-sepiolite materials with antimicrobial activities and low cytotoxicity. *Int J Biol Macromol*, 210: 337–349.

https://doi.org/10.1016/j.ijbiomac.2022.05.015

37. Ding H, Peng X, Yu X, *et al*., 2022, The construction of a self-assembled coating with chitosan-grafted reduced graphene oxide on porous calcium polyphosphate scaffolds for bone tissue engineering. *Biomed Mater*, 17: 045016.

https://doi.org/10.1088/1748-605X/ac6eab

38. Zhang R, Liu X, Xiong Z, *et al*., 2018, Novel micro/nanostructured TiO2/ZnO coating with antibacterial capacity and cytocompatibility. *Ceram Int*, 44: 9711–9719. https://doi.org/10.1016/j.ceramint.2018.02.202

39. Aljohani W, Ullah MW, Zhang X, *et al*., 2018, Bioprinting and its applications in tissue engineering and regenerative medicine. *Int J Biol Macromol*, 107: 261–275.

https://doi.org/10.1016/j.ijbiomac.2017.08.171

40. Bian T, Wang L, Xing H, 2021, Preparation and biological assessment of a ZrO2-based bone scaffold coated with hydroxyapatite and bioactive glass composite. *Mater Chem Phys*, 267: 124616.

https://doi.org/10.1016/j.matchemphys.2021.124616

41. Khosrowshahi A, Khoshfetrat AB, Khosrowshahi YB, *et al*., 2021, Cobalt content modulates characteristics and osteogenic properties of cobalt-containing hydroxyapatite in *in-vitro* milieu. *Mater Today Commun*, 27: 102392.

https://doi.org/10.1016/j.mtcomm.2021.102392

42. Wang S, Liu L, Zhou X, *et al*., 2019, Effect of strontium-containing on the properties of Mg-doped wollastonite bioceramic scaffolds. *Biomed Eng Online*, 18: 119.

https://doi.org/10.1186/s12938-019-0739-x

43. Rajkumar P, Sarma BK, 2021, Role of Zn and Mg substitutions on the mechanical behaviour of biomimetic hydroxyapatite and insight of the emergence of hydroxyapatite-ZnO nanocomposite. *Mater Charact*, 176: 111107.

https://doi.org/10.1016/j.matchar.2021.111107

44. Chen X, Zhang L, Liu X, *et al*., 2012, Preparation and properties of biodegradable composites derived from poly(lactide-co-glycolide), poly(L-lactide), and nanohydroxyapatite. *J Macromol Sci B*, 52: 462–475.

https://doi.org/10.1080/00222348.2012.712007

45. Mohajernia S, Hejazi S, Eslami A, *et al*., 2015, Modified nanostructured hydroxyapatite coating to control the degradation of magnesium alloy AZ31 in simulated body fluid. *Surf Coat Tech*, 263: 54–60.

https://doi.org/10.1016/j.surfcoat.2014.12.059

46. Shen Y, Liu W, Wen C, *et al*., 2012, Bone regeneration: Importance of local pH-strontium-doped borosilicate scaffold. *J Mater Chem*, 22: 8662–8670.

https://doi.org/10.1039/c2jm16141a

47. Rokusek D, Davitt C, Bandyopadhyay A, *et al*., 2005, Interaction of human osteoblasts with bioinert and bioactive ceramic substrates. *J Biomed Mater Res A*, 75: 588–594.

https://doi.org/10.1002/jbm.a.30459

48. Lian JB, Stein GS, 1992, Concepts of osteoblast growth and differentiation: basis for modulation of bone cell development and tissue formation. *Crit Rev Oral Biol Med*, 3: 269–305.

https://doi.org/10.1177/10454411920030030501

49. Silva AS, Santos LF, Mendes MC, *et al*., 2020, Multi-layer pre-vascularized magnetic cell sheets for bone regeneration. *Biomaterials*, 231: 119664.

https://doi.org/10.1016/j.biomaterials.2019.119664

50. Gregory CA, Gunn WG, Peister A, *et al*., 2004, An Alizarin red-based assay of mineralization by adherent cells in culture: Comparison with cetylpyridinium chloride extraction. *Anal Biochem*, 329: 77–84.

https://doi.org/10.1016/j.ab.2004.02.002

51. Wang X, Liu S, Li M, *et al*., 2016, The synergistic antibacterial activity and mechanism of multicomponent metal ions-containing aqueous solutions against *Staphylococcus aureus*. *J Inorg Biochem*, 163: 214–220.

https://doi.org/10.1016/j.jinorgbio.2016.07.019